Observed brightness distributions in overcast skies

Raymond L. Lee, Jr.,* and David E. Devan

Mathematics and Science Division, United States Naval Academy, Annapolis, Maryland 21402, USA

*Corresponding author: raylee@usna.edu

Beneath most overcasts, clouds' motions and rapidly changing optical depths complicate mapping their angular distributions of luminance L_v and visible-wavelength radiance L. Fisheye images of overcast skies taken with a radiometer-calibrated digital camera provide a useful new approach to solving this problem. Maps calculated from time-averaged images of individual overcasts not only show their brightness distributions in unprecedented detail, but they also help solve a long-standing puzzle about where brightness maxima of overcasts are actually located. When combined with simulated radiance distributions from MODTRAN4, our measured radiances also let us estimate the gradients of cloud thickness observed in some overcasts.   © 2008 Optical Society of America

OCIS codes: 010.1290, 010.1615, 010.5630, 010.7295, 120.5630, 290.1090.

1. Introduction

Popular and professional scientific works alike have long described the nonuniform brightness distribution of overcast skies [1,2], one version of which is the CIE's 1996 model of overcast luminance as a simple function of view-elevation angle [3]. Central to many such models is the assumption that, if short-term brightness fluctuations [4,5] are excluded, either luminance L_v or visible-wavelength radiance L is largest at and symmetric about the zenith in optically thick overcasts [6–9]. Indeed, several measurement campaigns have produced data that apparently support this assumption [9–13].

Yet doubts persist about it, ranging from suggestions that thick overcasts have nearly uniform luminances [14], to observations that some overcasts' brightness maxima are in fact not at the zenith [15–17], to an empirical model that predicts some slight zenith asymmetry even for thick overcasts [18,19]. More recently, the CIE has incorporated some of the asymmetry from [18] to allow for brightness maxima around the Sun in optically thin overcasts [20], as do several other empirical models [21–23]. Although most existing data lack the angular resolution and temporal smoothing needed to evaluate

all these competing claims [24,25], such problems are easily overcome with digital image analysis of overcasts photographed with a fisheye lens.

2. Brightness Calibration of a Skylight Camera

Consistent with our definitions of "overcast" elsewhere [26,27], here we analyze brightness distributions only in those cloudy skies for which (1) no clear sky is visible anywhere and (2) cloud cover is sufficiently optically thick that any cast shadows are indistinct. Although this definition does allow for overcasts with thin areas or a visible solar disk, nearly all skies that we analyzed qualify as densely overcast [16] ones in which the Sun was indiscernible. Our analysis is based on a wide variety of overcasts photographed from August 2006 to February 2008 at the U. S. Naval Academy (USNA) in Annapolis, Maryland. From 20 different overcasts, we acquired more than 1300 all-sky images by using a Nikon E5000 digital camera equipped with a Nikon FC-E8 fisheye converter lens. Although most of these overcast images were of nonprecipitating stratocumulus (Sc), stratus (St), and altostratus (As), we could also photograph during drizzle, light rain, and snow if we diligently sheltered and cleaned the lens.

Given that (1) cloud positions and optical depths τ change fairly rapidly during photography and (2) we are chiefly interested in the angular, rather than the

		Form Approved OMB No. 0704-0188

Report Documentation Page

1. REPORT DATE **APR 2008**	2. REPORT TYPE	3. DATES COVERED **00-00-2008 to 00-00-2008**

4. TITLE AND SUBTITLE **Observed brightness distributions in overcast skies**		5a. CONTRACT NUMBER
		5b. GRANT NUMBER
		5c. PROGRAM ELEMENT NUMBER
6. AUTHOR(S)		5d. PROJECT NUMBER
		5e. TASK NUMBER
		5f. WORK UNIT NUMBER
7. PERFORMING ORGANIZATION NAME(S) AND ADDRESS(ES) **United States Naval Academy (USNA),Mathematics & Science Department,Annapolis,MD,21402**		8. PERFORMING ORGANIZATION REPORT NUMBER
9. SPONSORING/MONITORING AGENCY NAME(S) AND ADDRESS(ES)		10. SPONSOR/MONITOR'S ACRONYM(S)
		11. SPONSOR/MONITOR'S REPORT NUMBER(S)

12. DISTRIBUTION/AVAILABILITY STATEMENT **Approved for public release; distribution unlimited**

13. SUPPLEMENTARY NOTES

14. ABSTRACT

15. SUBJECT TERMS

16. SECURITY CLASSIFICATION OF:			17. LIMITATION OF ABSTRACT	18. NUMBER OF PAGES	19a. NAME OF RESPONSIBLE PERSON
a. REPORT **unclassified**	b. ABSTRACT **unclassified**	c. THIS PAGE **unclassified**	**Same as Report (SAR)**	**12**	

Standard Form 298 (Rev. 8-98)
Prescribed by ANSI Std Z39-18

temporal, details of overcast brightness, on each day we took photographs every 30 s for ~30–40 min and then averaged these image sequences. At each pixel, this averaging reduces brightness fluctuations caused by short-term changes in cloud τ, fluctuations that can complicate the image analysis [28]. During each photography session, cloud advection usually results in several complete exchanges of clouds within the camera's 180° field of view (FOV). Although this smoothing eliminates the overcast's cloud-level details, it does preserve persistent features that are especially germane in evaluating the conflicting claims about overcast brightness distributions.

As described elsewhere, calibrating a digital camera to accurately record skylight L or L_v is now rather straightforward [27,29], as is determining how lens transmissivity and pixel position vary with zenith angle for a given fisheye lens. Note that because most overcasts have a limited range of colors, L and L_v differ by a near-constant scaling factor $L_v : L$ (typically, the standard deviation of $L_v : L < 0.5\%$ of its mean value). Thus the *shapes* (as opposed to the magnitudes) of meridional profiles of L_v and visible-wavelength L from 400 to 700 nm will not differ appreciably for a given overcast. In a variation on the spectral calibration procedure described in [27], we define a 1×3 L or L_v transform matrix $\mathbf{G}$ as

$$\mathbf{G} = \mathbf{B}\rho^{\mathbf{T}}(\rho\rho^{\mathbf{T}})^{-1}, \tag{1}$$

where $\mathbf{B}$ is a $1 \times n$ matrix of n different skylight radiances or luminances measured with a Photo Research PR-650 radiometer [30] (the training set of data), ρ is the corresponding $3 \times n$ matrix of normalized 12 bit/channel RGB pixel values for the same n features, and $\rho^{\mathbf{T}}$ is ρ's transpose. Each of the n RGB triplets in ρ (i.e., each column) is multiplied by a different scaling factor F that is proportional to the corresponding image's scene irradiance, and F is calculated from each image's photographic exposure value [31]. Our radiance training set includes L data from five different overcasts, and it has $n = 232$ features of widely varying color and brightness. To use the resulting least-squares transform matrix $\mathbf{G}$, we photograph a new overcast feature with the camera still operating in its 12 bit/channel RAW mode. This new feature's reconstructed L is the only element of the 1×1 matrix $\mathbf{B_r}$ given by

$$\mathbf{B_r} = \mathbf{G}\rho_{\mathbf{r}}, \tag{2}$$

where $\rho_{\mathbf{r}}$ is the feature's 3×1 matrix of RGB pixel values. Similar to our scaling of ρ's columns, each $\rho_{\mathbf{r}}$ in a time-averaged image is scaled by an irradiance factor F based on that image's mean exposure value. As a result of this scaling, Eq. (2) yields absolute rather than relative L and L_v. According to Photo Research, at specified radiance levels a properly calibrated PR-650 radiometer measures L and L_v accurate to within $\pm 4\%$. We make the conservative assumption that such errors follow a uniform random

distribution (i.e., this will overestimate many radiometer L errors). If this assumption is applied to a set of camera and radiometer data *not* used to calculate $\mathbf{G}$, then Eq. (2)'s root-mean-square errors in absolute reconstructed L and L_v are $< 5.8\%$.

Beyond these purely radiometric calibrations are two geometric ones. First we measure how light rays incident at angles θ_i from the FC-E8 fisheye lens' optical axis are mapped onto the camera sensor. Knowledge of this angular mapping or projection is needed to convert a pixel's radial distance from the center of an all-sky image into the corresponding sky zenith angle θ. A normalized version of this pixel distance is $r_n = r_{\text{abs}}/r(\theta_i = 90°)$, where r_{abs} is the Cartesian pixel distance from a target pixel to the one at the lens' optical axis and $r(\theta_i = 90°)$ is the pixel distance from that axis to pixels at $\theta_i = 90°$. Thus $0 \le r_n \le 1$ for any pixel in an all-sky image that is at or above the astronomical horizon.

To perform this geometric calibration, we mount the camera and fisheye lens on an optical stage free to rotate about a vertical axis that intersects the lens' nodal point. Next we position a point light source at the same height as the lens' optical axis and several meters from the camera. Then we photograph this light source in darkness as we rotate the stage in 1° steps. By relating the light's changing pixel position to the lens' rotation angle, we establish Fig. 1's mapping of $\theta_i(r_n)$. The FC-E8 lens' slightly nonlinear $\theta_i(r_n)$ is close to the equisolid angle fisheye projection $[\sin(\theta_i/2) \propto r_n]$, which is intermediate to the equidistant ($\theta_i \propto r_n$) and orthographic $[\sin(\theta_i) = r_n]$ projections [32].
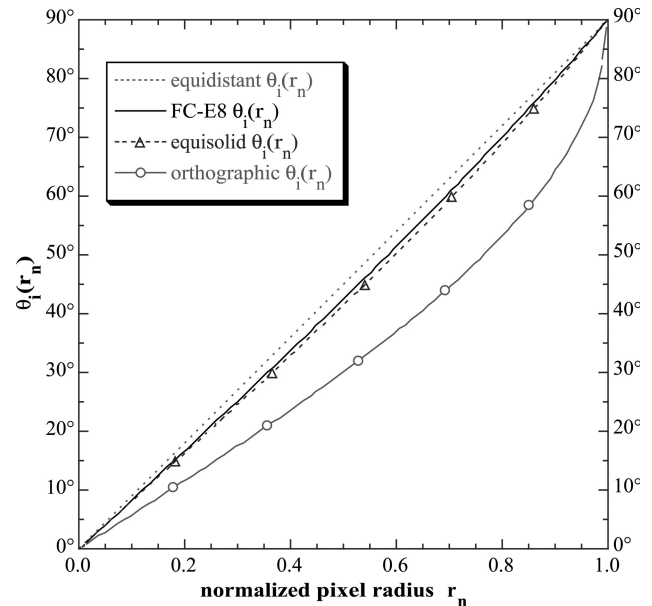

Fig. 1. Angular mappings for various fisheye lens projections, where θ_i is the angle between a lens' optical axis and an incident light ray, and r_n is the normalized radius from the image's center to the pixel illuminated by that ray. The FC-E8 curve is the measured mapping for our particular model of Nikon fisheye lens.

Our second geometric calibration also has a radiometric component. Equisolid angle fisheye lenses are designed so that each sensor pixel images a solid angle of the same size. Thus if *only* a pixel's FOV governed its irradiance E, then pixel E would be independent of θ_i for an isotropic radiance field. Because the FC-E8's angular projection is not quite equisolid, the solid angle subtended by (and thus E on) its sensor pixels decreases slightly toward the image's edge. Compounding this smaller *illumination factor* at larger θ_i are increased optical path lengths within and external reflectances from the lens' glass elements. As θ_i increases, the associated decreases in transmitted light also reduce pixel E.

To correct for these losses, we map their combined effects in Fig. 2 as the lens' effective transmissivity T_{eff} [also called its $L(\theta_i)$ *rolloff* [33]]. To calculate T_{eff}, we first photograph at close range a diffusely lit diffuse reflector (a matte-finish photographer's gray card outside on an overcast day) that spans much of the FC-E8's approximately 180° FOV [34]. Because the card's reflected L are quite spatially uniform for such illumination, any changes in image gray levels measured radially from the optical axis are due to the lens itself. Figure 2 shows a smoothed, normalized version of this radial profile of our isotropic card's image brightnesses, which are themselves proportional to T_{eff}. The small local maximum in T_{eff} at $\theta_i \sim 17.8°$ [note that $T_{\text{eff}}(0°) = 0.9898$] is partly explained by the combined effects of the nonabsorbing Fresnel transmissivity and our fisheye lens' illumination factors as functions of θ_i; others have also measured T_{eff} maxima at $\theta_i > 0°$ [33]. Our tests reveal no appreciable changes in $T_{\text{eff}}(\theta_i)$ ar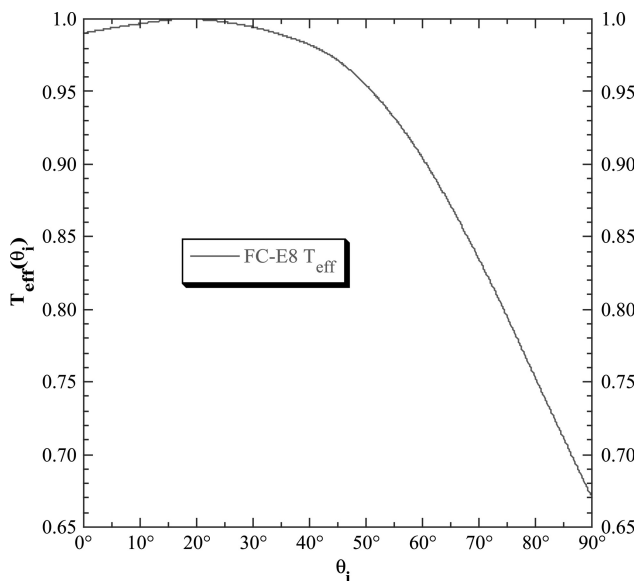ound the FC-E8's optical axis. Once we know an image pixel's θ_i, we can correct its brightness by dividing the original L or L_v by the corresponding value of $T_{\text{eff}}(\theta_i)$.

3. Measuring Angular Details of Overcast Brightness

A. All-Sky Maps of Overcast Radiance

We take two tacks here in analyzing overcast brightness distributions: (1) binning the corrected L to produce all-sky maps and (2) plotting profiles of azimuthally averaged L or L_v as functions of sky zenith angle θ. To explain the former technique, we begin with Fig. 3's image of a Sc overcast taken on 4 April 2007. Figure 3 is a gray-scale version of the average 12 bit/channel color image that we calculated from 83 individual photographs of this overcast. Although we have made no geometric or radiometric corrections to its pixel gray levels, Fig. 3 clearly conveys the impression that the circumzenithal region is the brightest part of the sky.

Figure 4 quantifies this impression with a map of Fig. 3's relative radiances L_{rel} that have been corrected for $T_{\text{eff}}(\theta_i)$ and then binned into 5% intervals. A legend indicates the gray-scale encoding of L_{rel}, which can be converted to absolute radiances by multiplying it by Fig. 4's maximum radiance L_{max}. Figure 4 and all subsequent L_{rel} maps preserve Fig. 3's essentially equisolid projection of $\theta_i(r_n)$. The zenith is marked by a black +, and two small black squares near the 6 o'clock position show the limits of the Sun's position during photography. Figure 4 lists other relevant details, including the photographic session's time interval Δt and range of unrefracted Sun elevations h_0.

Fig. 2. Normalized effective transmissivity T_{eff} as a function of θ_i measured for our FC-E8 fisheye lens. T_{eff} accounts for all radiance losses at the image sensor due to the camera optics, including illumination factors, external and internal reflections, and absorption within the lens.
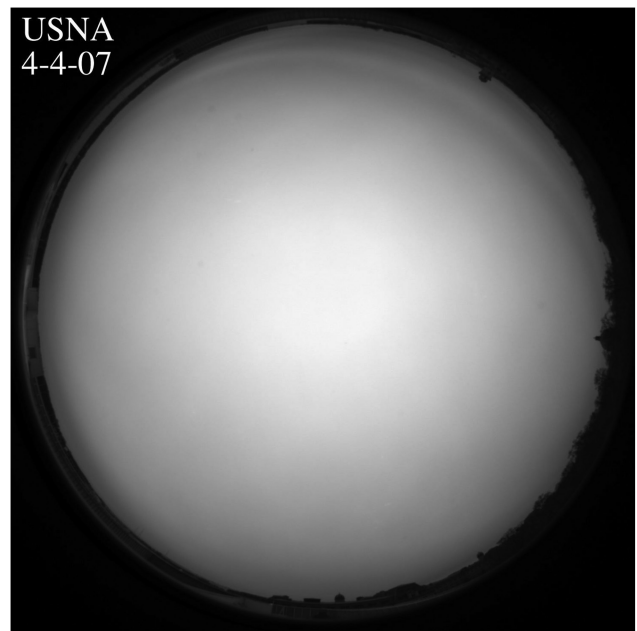

Fig. 3. Gray-scale version of a time-averaged color image of a stratocumulus (Sc) overcast photographed at USNA in Annapolis, Maryland on 4 April 2007. Averaging of small-scale details in the 83 individual photographs that comprise Fig. 3 makes this Sc overcast resemble stratus (St).
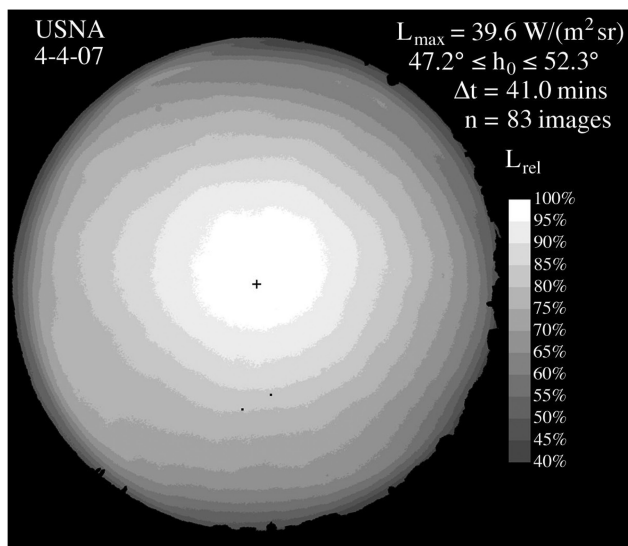
Fig. 4. Map of binned relative radiances L_{rel} calculated from Fig. 3 by using Eqs. (1) and (2) and corrected for brightness rolloff in the original image. L_{rel} is Fig. 3's absolute L in W/(m^2 sr) normalized by its maximum radiance L_{max}. A black + marks the zenith, and two small black squares near the 6 o'clock position show the limits of the Sun's position during photography. This and subsequent maps of L_{rel} include details about the underlying mean image and its corresponding range of unrefracted Sun elevations h_0.

As expected from [6–13], Fig. 4's largest L occur near the zenith. Yet these 95th-percentile L_{rel} are not exactly centered on it, nor is the rest of the 4 April 2007 radiance field especially symmetric (i.e., L_{rel} values are not constant along almucantars). Note in particular that most L_{rel} contours are wider to the left of the zenith for $\theta < 70°$. Because the Sun's disk was never visible through the 4 April 2007 overcast, we know that its cloud cover was optically thick. Thus we cannot attribute this overcast's mild asymmetry in L_{rel} to the kind of direct-beam scattering simulated by the 2003 CIE model [20]. We define an overcast's *asymmetry axis* as the line that passes through the center of its 95th-percentile L_{rel} and the zenith, assuming that these two points differ. Contrary to the CIE model's assumption, Fig. 4's asymmetry axis is rotated ~45° clockwise from the Sun–zenith axis, the projection of the single-scattering *principal plane* onto an all-sky image.

In fact, Fig. 4's entire radiance distribution is skewed with respect to this axis, a scattering pattern not seen in clear skies. Yet even moderately thick (say, vertical thickness $h \sim 0.5\,km$) overcasts make photons undergo many more scatterings before reaching the surface than do cloud-free atmospheres, so their brightness patterns should differ greatly from clear-sky ones. Multiple scattering in dense overcasts, especially when combined with our temporal averaging, will make droplet properties such as single-scattering albedo or asymmetry parameter contribute negligibly to these patterns. Overcasts with more symmetric L_{rel} contours such as Fig. 5 also can have a distinctly noncircular region of maximum
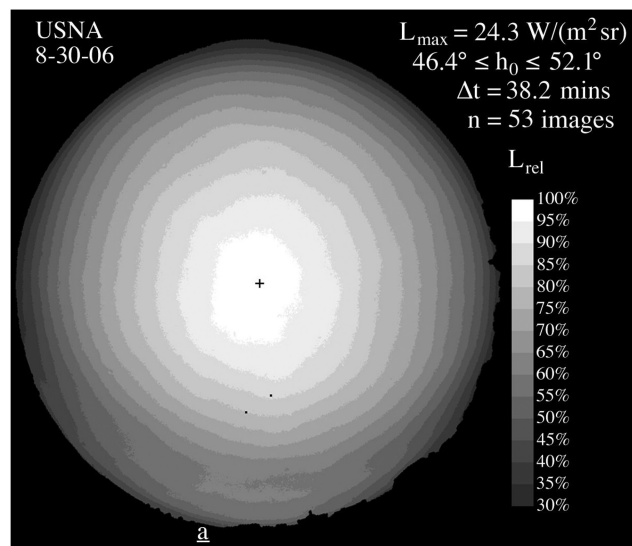

Fig. 5. Map of binned L_{rel} calculated from the time-averaged color image [Fig. 4(a) in [27]] of a Sc overcast photographed at USNA on 30 August 2006.

radiance around the zenith. Recall that all our maps of binned L_{rel} are averages of ~30 min, so such asymmetries are far from momentary.

Still other kinds of irregular features can occur, such as Fig. 6's region of 95th-percentile L_{rel} that is neither circular nor centered on the zenith. As in Fig. 4, this feature's asymmetry axis does not align with the mean Sun–zenith axis. In all maps, the latter axis extends straight down from the zenith +, while the asymmetry axis in Fig. 5 extends from the zenith to the horizon position a. The routine misalignment of these two axes suggests that some property of a dense overcast *other* than its mean optical depth governs the asymmetry pattern of L_{rel}.
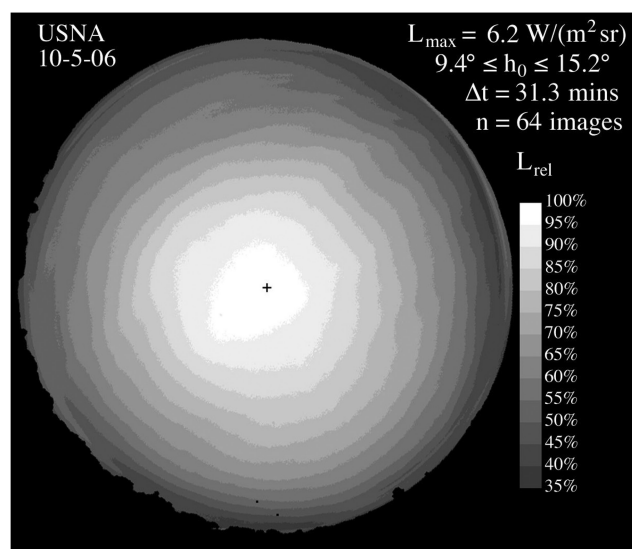

Fig. 6. Map of binned L_{rel} calculated from the time-averaged color image of a Sc overcast photographed at USNA on 5 October 2006.
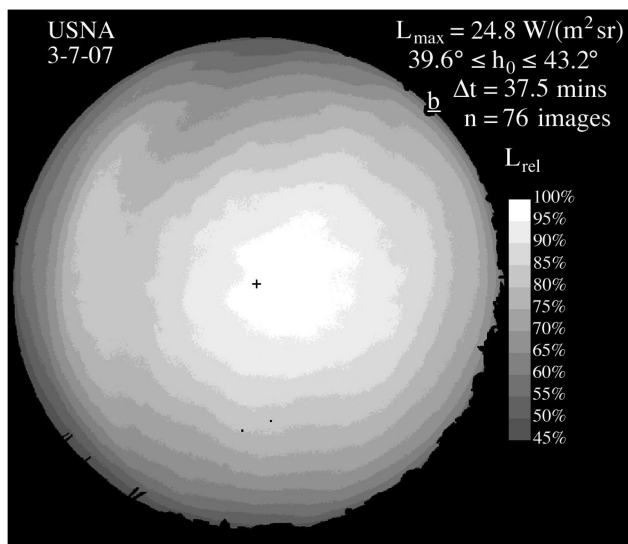
Fig. 7. Map of binned L_{rel} calculated from the time-averaged color image of a Sc overcast photographed at USNA on 7 March 2007. Unlike other days at our site, snow was falling then and covered the surrounding terrain.

Fig. 9. Map of binned L_{rel} calculated from the time-averaged color image of a Sc overcast photographed at USNA on 12 February 2008.

As further evidence of this, Fig. 7's map of L_{rel} on 7 March 2007 shows an optically thick overcast whose asymmetry axis is even more misaligned with the principal plane. On this day light snow was falling that covered our site and surrounding terrain to a depth of ~10 cm. Although this high-albedo surface helped reduce the range of observed L_{rel} to ~2.14∶ 1, it did nothing to make the distribution of overcast L_{rel} more regular, as indicated by its asymmetry axis at approximately the 2 o'clock position. Yet before making too much of snow cover's effects, note that Fig. 8's snow-free overcast has an asymmetry axis in roughly the same compass direction. Thus in Figs. 7 and 8, lines drawn from the zenith to the same
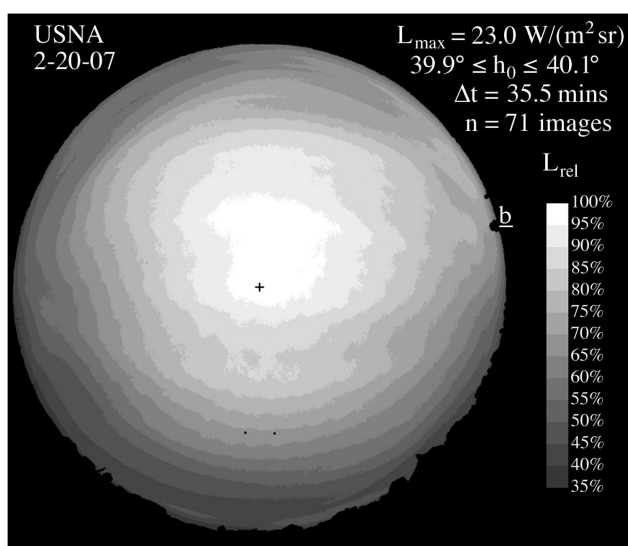
horizon feature b̲ are both close to their overcasts' respective asymmetry axes. Other snow-free overcasts (e.g., Fig. 9) have their regions of maximum L_{rel} displaced just as far into the antisolar sky as does Fig. 8. So at least in our measurements, the distribution of L in dense overcasts is little affected by large variations in surface albedo, although these are important in phenomena such as polar *ice blink* or *snow blink* [35].

Even in overcasts where the Sun's disk is occasionally visible, the region of maximum L_{rel} may not surround the Sun's position or even be at its azimuth. Figure 10 illustrates the latter case for an overcast where the Sun's disk dimly appears in 14 of 67 photographs. Here the principal plane is ~25° from the L_{rel}

Fig. 8. Map of binned L_{rel} calculated from the time-averaged color image of a Sc overcast photographed at USNA on 20 February 2007.
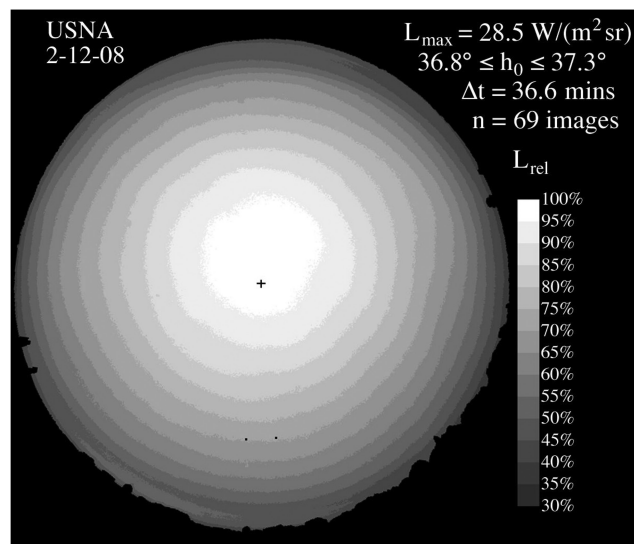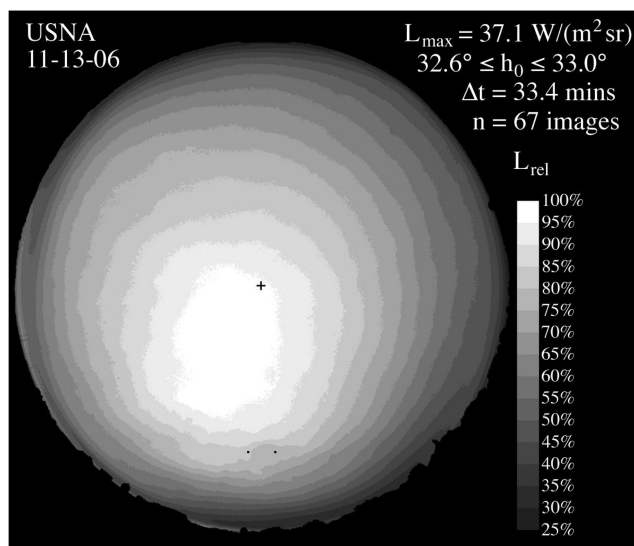

Fig. 10. Map of binned L_{rel} calculated from the time-averaged color image of a Sc overcast photographed at USNA on 13 November 2006.
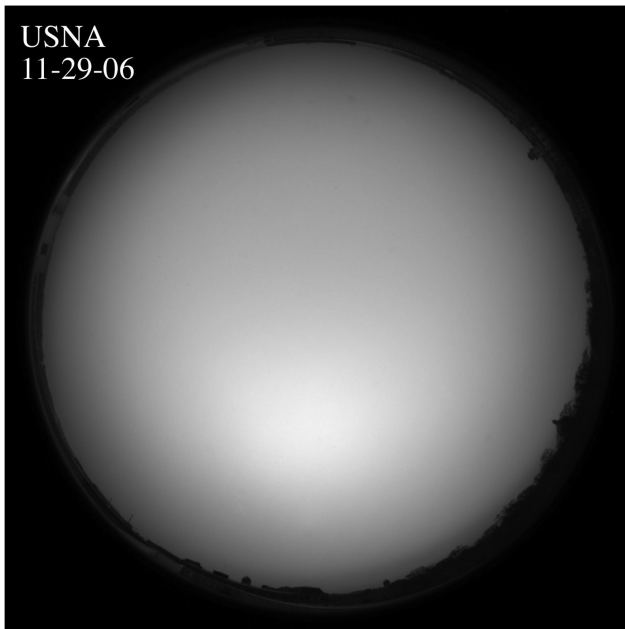
Fig. 11. Gray-scale version of the time-averaged color image of a Sc overcast photographed at USNA on 29 November 2006.

asymmetry axis, the simplest explanation for which is that Fig. 10's clouds tend to be thinner there. In Fig. 11's mean gray-scale image of another Sc overcast, the Sun's disk is just perceptible in an even smaller fraction of the underlying photographs (9 of 65). In Fig. 12's corresponding radiance map, the region of maximum L_{rel} straddles the principal plane, yet it still does not surround the Sun (black squares near the 6 o'clock position). Thus even in some thin overcasts, no simple relationship exists between the positions of L_{rel} maxima and the Sun.

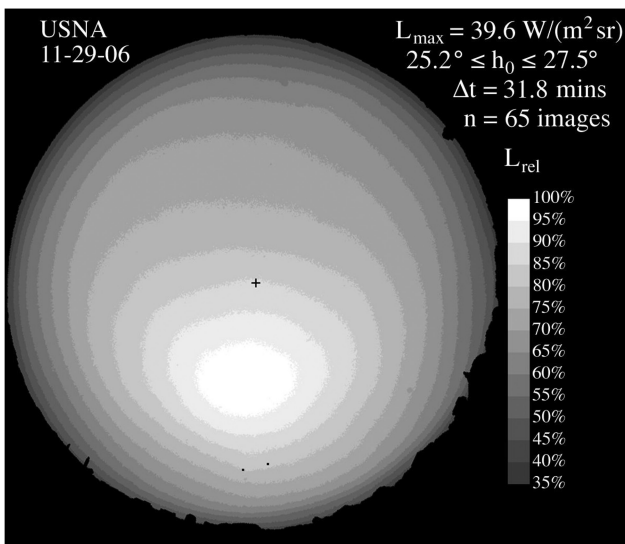Table 1 summarizes these L_{max} details for 19 different overcasts (it excludes one whose radiances

Fig. 12. Map of binned L_{rel} calculated from Fig. 11's color original. Note that the brightest area of this occasionally thin overcast lies between the zenith and Sun, which is just visible in ∼14% of the individual photographs that comprise Fig. 11.

were measured through a linear polarizer). In our maps of L_{rel} (Figs. 4–10 and 12), note that L_{max}'s zenith angle θ and azimuth relative to the Sun ϕ_{rel} need not be at the center of the overcast's 95th-percentile radiances. Note too that ϕ_{rel} is measured counterclockwise from the Sun's azimuth in these maps because we are looking up at the sky rather than down at the surface. Rows in Table 1 are sorted in order of increasing $\theta(L_{max})$, meaning that these overcasts exhibit progressively less zenithal symmetry toward the bottom of the table.

In fact, if we exclude Table 1's last three rows, consisting of overcasts with bright (and thus optically thin) horizons, the mean value of $\theta(L_{max}) = 11.15°$, the median $\theta(L_{max}) = 7.12°$, and its standard deviation $s = 9.62°$. Using the same criterion for $\phi_{rel}(L_{max})$, its mean $= 197.25°$ and $s = 117.93°$. A t test of the $\theta(L_{max})$ departures from $0°$ indicates that they are significant at the $\alpha = 0.016\%$ level. In addition, L_{max} is nearly independent of Sun position: the magnitude of the linear correlation coefficient R between $\theta(L_{max})$ and mean h_0 is <0.12. Thus, by both visual and statistical standards, optically thick overcasts do not have L_{max} at the zenith, nor do their L_{rel} asymmetry axes have any consistent orientation.

B. Azimuthally Averaged Profiles of Overcast Brightness

In the past, many researchers have depicted overcast brightness trends by using meridional profiles of L or L_v rather than all-sky maps [2,11,16,17,24,25]. Depending on the technology then available, such profiles may consist of radiometer measurements at only a few θ, and these may or may not be azimuthally averaged. Digital imaging's wealth of high-resolution angular detail avoids such limitations, and it makes possible entirely new ways of analyzing overcast brightness. Yet because meridional profiles of azimuthally averaged L and L_v remain a convenient and conventional analytical tool, we give several examples here. Our earlier caveat still holds: brightness in most overcasts is not constant along almucantars, so azimuthal averaging of L or L_v tacitly assumes a symmetry that seldom exists.

Figure 13 compares the daytime L_v profile of a typical clear sky with those for an As and a Sc overcast; the conventional meteorological abbreviations CLR and OVC indicate the sky state. In Fig. 13 and all subsequent profiles, overcast brightnesses are averaged across all azimuths (i.e., $0° \leq \phi_{rel} < 360°$). However, Fig. 13's clear-sky average is confined to two $90°$ wide sectors that are symmetric about the clear-sky principal plane (i.e., $45° \leq \phi_{rel} \leq 135°$ and $225° \leq \phi_{rel} \leq 315°$); so its L_v exclude the solar and antisolar regions. From the zenith to within a few degrees of the horizon, the clear-sky L_v increase monotonically much as they would in a purely molecular atmosphere [36]. However, L_v decreases for $\theta > 88°$, and this local maximum occurs because scattering within the near-surface layers decreases direct sunlight's radiance enough to offset the corresponding gains

Table 1.   Sun Elevations for and Positions of Overcast Radiance Maxima

Figures	Date	Cloud Type	h_0 Interval[a] (deg)	L_{max} (W/m^2 sr)	$\theta(L_{max})$ (deg)	$\phi_{rel}(L_{max})$ (deg)
13, 14	20 Aug. 2007	Sc	62.7–59.7	40.11	1.60	259.86
	9 Nov. 2007	Sc	15.6–10.1	5.93	2.54	274.58
15	26 Nov. 2007	St	27.6–24.7	14.9	2.86	247.48
3, 4, 21	4 Apr. 2007	Sc	47.2–52.3	39.65	4.02	38.69
5, 16	30 Aug. 2006	Sc	46.4–52.1	24.35	4.44	244.06
9, 20	12 Feb. 2008	Sc	36.8–37.3	28.52	5.86	176.15
6	5 Oct. 2006	Sc	15.2–9.4	6.19	6.45	334.24
	25 Oct. 2007	Sc	15.9 – 10.7	2.61	6.84	348.21
	14 Sept. 2007	Sc	53.0 – 50.6	33.33	7.40	20.55
7, 16	7 March 2007	Sc	39.6–43.2	24.76	10.85	98.84
	19 Nov. 2007	St	30.1–27.6	13.44	11.48	212.84
13	29 Jan. 2008	As	31.8–32.5	27.66	11.76	44.69
10, 17	13 Nov. 2006	Sc	32.6–33.0	37.09	17.97	303.43
8	20 Feb. 2007	Sc	40.1–39.9	22.98	24.41	166.31
	23 Aug. 2007	Sc	30.5–37.2	20.00	25.42	34.69
11, 12, 17	29 Nov. 2006	Sc	25.2 – 27.5	39.61	34.55	351.40
	5 Feb. 2008	As	33.9–34.5	37.62	69.22	25.50
	13 Sept. 2006	Sc	48.6–51.6	28.55	77.20	156.93
	12 Jan. 2007	Sc	27.6–29.1	31.31	82.94	332.29

[a]Morning observations list the smaller h_0 value first, whereas afternoon observations list it last.

Fig. 13.   Meridional profiles of skylight luminance L_v as a function of sky zenith angle θ at USNA for one clear sky (labeled CLR) and two overcasts (labeled OVC). $L_v(\theta)$ in each profile are averaged over all relative azimuths ϕ_{rel} at fixed θ. Although the near-horizon brightness maximum in the clear sky is fairly well understood [37], similar extrema in overcasts are not.

in skylight that is multiply scattered toward us [25,37].

In contrast, both overcasts in Fig. 13 become progressively darker as θ increases, as expected from the meridional patterns of Figs. 3–12. Although one clear-sky profile of L_v largely resembles another, daily changes in the slopes and details of overcast $L_v(\theta)$ are pronounced. For example, the ratio of maximum:minimum L_v is 2.49:1 on 29 January 2008, but it decreases to 2.12:1 on 20 August 2007, ratios similar to those predicted by some of the earliest overcast models [2,3].

Yet this expected feature of L_v decreasing with increasing θ is joined by an entirely new and unexpected one: near the horizon are paired local minima and maxima in both overcasts' L_v, a common overcast detail that is unexplained by existing radiative transfer models. The image underlying Fig. 13's 20 August 2007 profile is Fig. 14, and its luminance
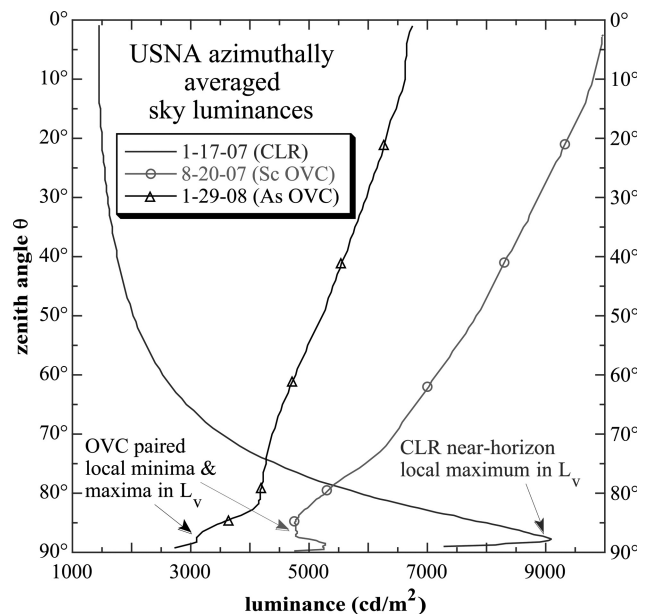
banding near the horizon seems to be the result of perspective compression of parallel striations in the time-averaged τ [27]. In fisheye photographs, these alternating bright and dark bands in the mean low-level flow resemble barrel staves. Like barrel staves, the bands become visually compressed near
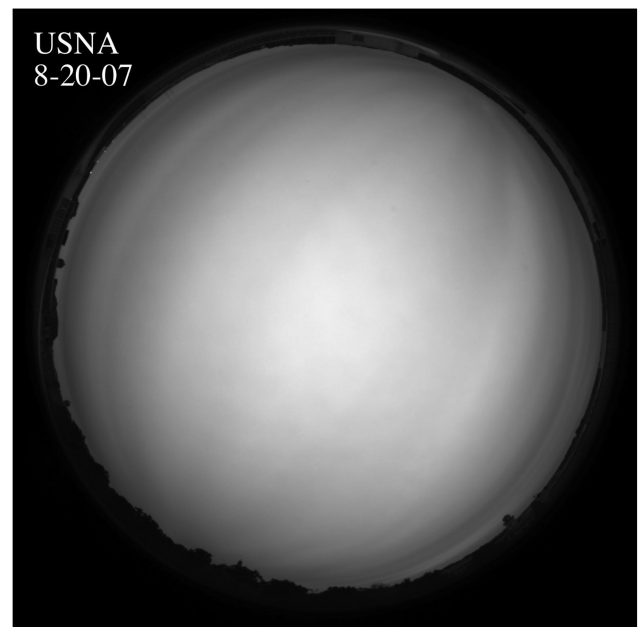

Fig. 14.   Gray-scale version of the time-averaged color image of a Sc overcast photographed at USNA on 20 August 2007. The alternating bright and dark bands are caused by persistent minima and maxima in overcast optical depth that parallel the mean low-level flow.

the horizon and so cause the kind of angularly narrow maxima and minima plotted in Fig. 13.

Figure 15 supports our claim in Section 2 that in a given overcast the meridional profiles of L_v and visible-wavelength L will have nearly the same shape. This correspondence between luminance and radiance will be closest in those overcasts with limited color gamuts, because the more dissimilar the shapes of an overcast's visible spectra are, the larger will be both the differences in its colors and L_v:L ratios.

Thus Figs. 16 and 17 show the same patterns in overcast L as Fig. 15 does in L_v: the maximum azimuthally averaged L occurs at the zenith, and L steadily decreases to within a few degrees of the horizon. As in Fig. 13, most of the Fig. 16 and 17 overcasts have closely paired local minima and maxima in L for $\theta > 85°$. However, the time-averaged image of the 29 November 2006 overcast (Fig. 11) shows none of the striations that readily explain the near-horizon L behavior of the other overcasts. Close scrutiny of Fig. 11's horizon reveals only gradual variations in brightness as the cause of Fig. 17's local minimum at $\theta = 88.25°$.

Plausible physical explanations of these local minima–maxima pairs include that (1) as θ increases near the horizon, subcloud airlight scattering reverses the trend of decreasing L caused by steady increases in overcast slant-path τ (i.e., the local minimum), which is followed by (2) greater surface-based absorption of this airlight at the largest θ where scattering paths are closest to the ground (i.e., the local maximum). In scenario (2), multiple scattering is effectively reduced because of short single-scattering distances to the absorbing surface.
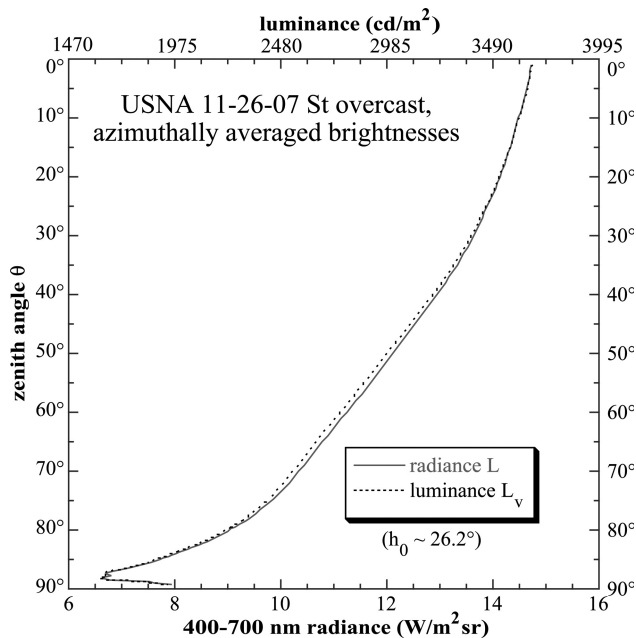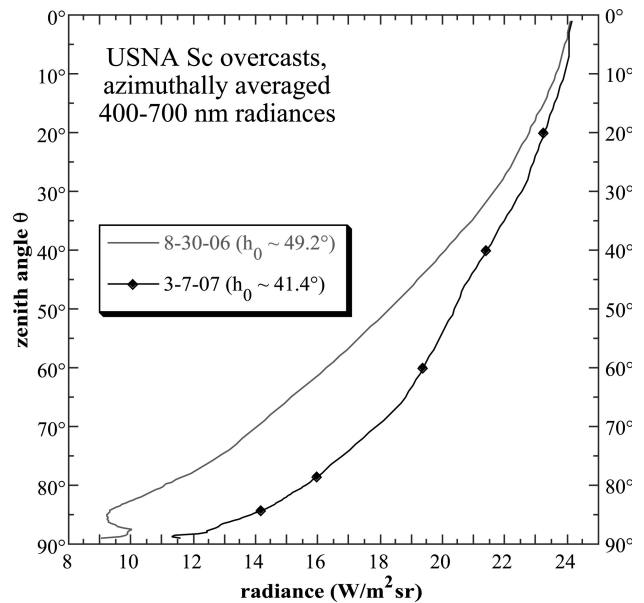

Fig. 16. Meridional profiles of $L(\theta)$ averaged across all ϕ_{rel} for two overcasts at USNA on 30 August 2006 and 7 March 2007. Compare these profiles with the corresponding all-sky maps of L_{rel} (Figs. 5 and 7, respectively).

Tentative evidence for this logic comes from the snow-covered day of 7 March 2007 (Fig. 16), for which there is *no* local maximum in $L(\theta)$ just above the horizon. Yet the same holds true for the snow-free day of 26 November 2007 (Fig. 15), so the issue seems unresolved for now.

4. Cloud Thickness Gradients and Overcast Brightness Asymmetries

What displaces overcast brightness maxima from the zenith, a displacement that seems independent of

Fig. 15. Meridional profiles of radiance $L(\theta)$ and luminance $L_v(\theta)$ averaged across all ϕ_{rel} for the same St overcast. In most daytime overcasts, the ratio $L_v(\theta)$:$L(\theta)$ is nearly constant.
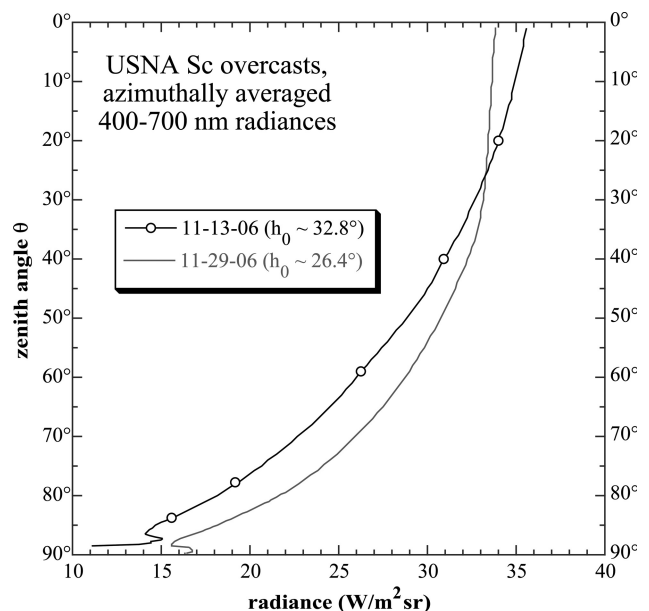

Fig. 17. Meridional profiles of $L(\theta)$ averaged across all ϕ_{rel} for two overcasts at USNA on 13 November and 29 November 2006. Compare these profiles with the corresponding all-sky maps of L_{rel} (Figs. 10 and 12, respectively).
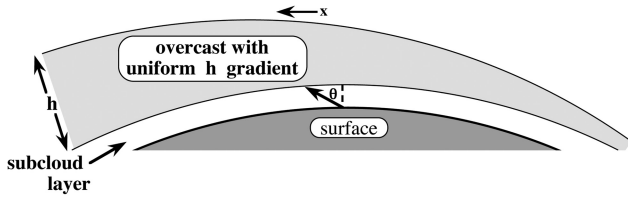
Fig. 18. Schematic cross section of an overcast with vertical geometric thickness h that increases nearly linearly in the direction x. In our calculations, we make this gradient $\Delta h/\Delta x$ constant in magnitude and direction. Overcast thickness and curvature are exaggerated here; θ is the sky zenith angle for a surface-based observer.

Sun position (see Table 1)? This is the fundamental question implicit in Figs. 3–12, and Fig. 18 provides one answer. This schematic cross section of an overcast adds a new feature to existing models' explicit or implicit picture of a uniform cloud deck: a constant, unidirectional gradient of cloud thickness h.

The instantaneous distribution of overcast h and its corresponding effects on ground-level irradiances and radiances can be complicated indeed [38–42]. However, the overcast images that underlie our L_{rel} maps (Figs. 4–10 and 12) are 30–40 min averages of scores of individual photographs, and so these maps are dominated by only the most persistent cloud inhomogeneities. In particular, advection of the cloud field above our site greatly reduces each L_{rel} map's range of averaged h and thus its horizontal gradients of h. This pronounced smoothing lets us realistically adapt an explicitly horizontally homogeneous model such as MODTRAN4 [43] to estimate how changes in h might affect the angular distribution of overcast L.

To make this adaptation, we compute tables of MODTRAN's overcast L as functions of h and θ for the combination of solar h_0, cloud type, and cloud base height z_{base} observed during each of several different overcasts [44]. Because MODTRAN absolute radiances vary negligibly with ϕ_{rel} for $h > 0.5\,\mathrm{km}$, we can interpolate within these tables to estimate how MODTRAN's predicted L_{rel} depend on θ and h at all ϕ_{rel} (recall that L_{rel} is absolute L in $\mathrm{W}/(\mathrm{m}^2\,\mathrm{sr})$ scaled by an image's maximum radiance L_{max}). We assume that within the camera's FOV (1) z_{base} is constant and (2) a linear gradient $\Delta h/\Delta x$ can be substituted for the true curvilinear gradient above a spherical earth. However, neither of these reasonable assumptions is crucial to our results below.

Figure 19 shows the effects on L_{rel} of changing from uniform h [Fig. 19(a)] to a small, constant $\Delta h/\Delta x$ [Fig. 19(b)]. These maps of simulated MODTRAN radiances are based on Fig. 9's measured h_0 and z_{base}. If h is not spatially uniform, then Fig. 19(a)'s pattern of azimuthally symmetric L_{rel} shifts away from the zenith and develops a slight asymmetry axis at the ϕ_{rel} where $\Delta h/\Delta x$ intersects the zenith [Fig. 19(b)]. As expected, this gradient is quite small, having a value of $\sim$0.00155 or $<$0.1°. These values assume that the total horizontal distance across our 180° FOV is twice the tangent-line distance from our site to Fig. 9's observed $z_{base} = 1.4\,\mathrm{km}$; actual horizontal visibility distances to the cloud base will be smaller. Although we cannot reproduce all of Fig. 9's details with Fig. 19(b)'s simple unidirectional h gradient, adding it to Fig. 19(a) clearly makes for a much more realistic map.

A natural corollary to Fig. 19(b)'s simulated distribution of $L_{rel}(\theta, \phi_{rel})$ given h is a map of estimated h given the measured $L(\theta, \phi_{rel})$. To calculate such a map, we start with the values of $L(\theta, \phi_{rel})$ at each pixel in the time-averaged image used to generate Fig. 9. Then we interpolate at fixed θ within the appropriate MODTRAN tables of $L(\theta, h)$ to find the value of h that corresponds to each of these observed radiances. For $h > 0.5\,\mathrm{km}$ and fixed θ, MODTRAN L decrease monotonically as h increases. Thus once a pixel's θ
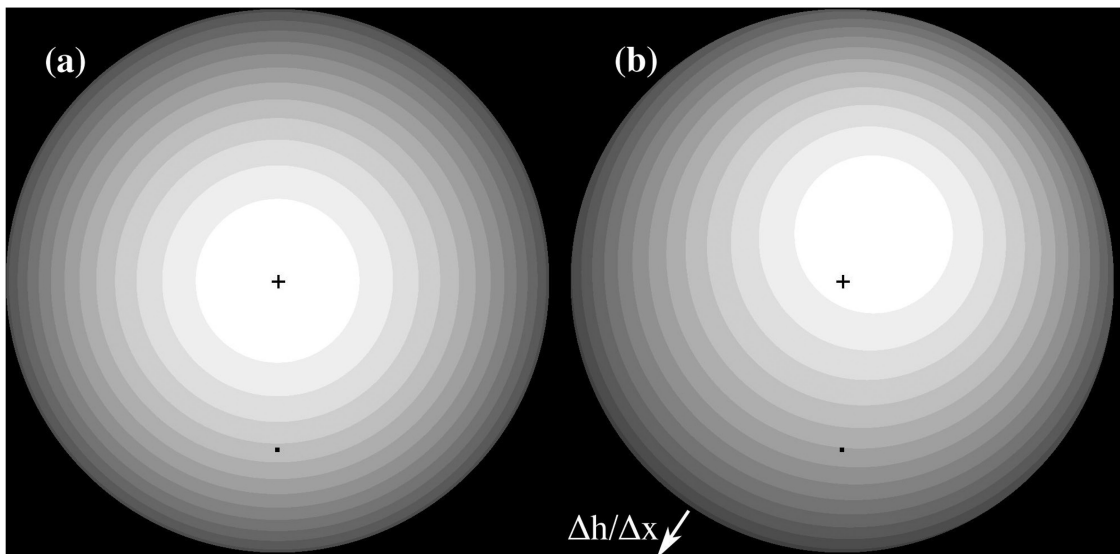

Fig. 19. MODTRAN4 simulations of L_{rel} in a Sc overcast with (a) constant $h = 0.894\,\mathrm{km}$ and (b) constant, unidirectional $\Delta h/\Delta x = 0.00155$ ($\sim$0.089°) at an angle of 34° from the principal plane. The L_{rel} scale here is the same as in Fig. 9, and h increases from 0.687 to 1.101 km over a horizontal distance that is twice the tangent-line distance from our site to Fig. 9's observed $z_{base} = 1.4\,\mathrm{km}$.

is calculated in a dense overcast, we can use the model $L(\theta, h)$ to identify its vertical thickness h uniquely. Of course, for an overcast that actually has multiple discrete layers, this h value will only be an equivalent thickness.

In Fig. 20 we estimate the actual h distribution existing during Fig. 9's measurements on 12 February 2008. Not surprisingly, Fig. 20's h pattern is much more complicated than that in Fig. 19(b), which assumed an h gradient having only *one* direction and magnitude. That said, the measured gradient's trend of decreasing h at $\phi_{rel} \sim 130°$ is clear in Fig. 20 (look from the zenith toward location $\underline{c}$), and its orientation is reasonably close to the $\phi_{rel} = 146°$ direction of $-\Delta h/\Delta x$ chosen for Fig. 19(b). We estimated the latter direction purely visually from Fig. 9, and so we should not expect perfect agreement between the two gradient orientations. However, much of the difference arises from other h gradients present in Fig. 20, and the combined result of these is a net h gradient that nearly parallels the principal plane.

Figure 21 shows the distribution of h observed for Fig. 4's overcast of 4 April 2007, and here the net h gradient is even easier to see along an axis $\sim 45°$ clockwise from the principal plane. This h gradient manifests itself in Fig. 4 as its L_{rel} asymmetry axis. Although the spacing of h contours in Fig. 21 may seem smaller than in Fig. 20, in fact the magnitudes of these gradients differ relatively little. First, the figure legends in Figs. 20 and 21 show that their ranges of observed h are nearly equal. Second, the apparently larger h gradient on Fig. 21's left side is actually due to perspective compression of radial distances at the cloud base as θ increases. Clearly these figures provide only estimates of h, and their reliability depends on the accuracy of both our mea-
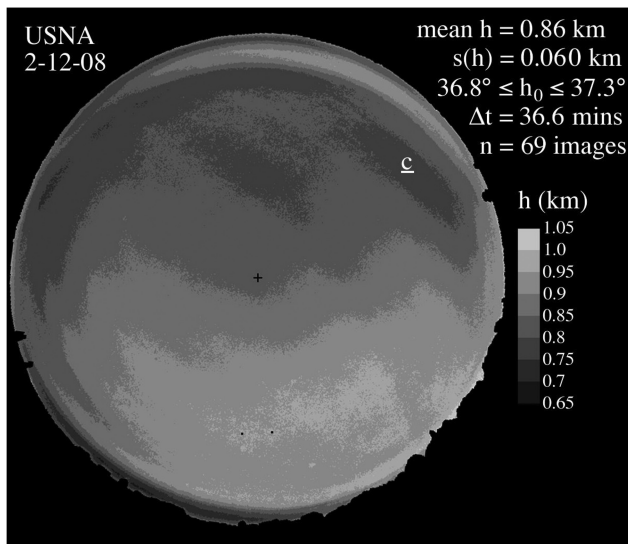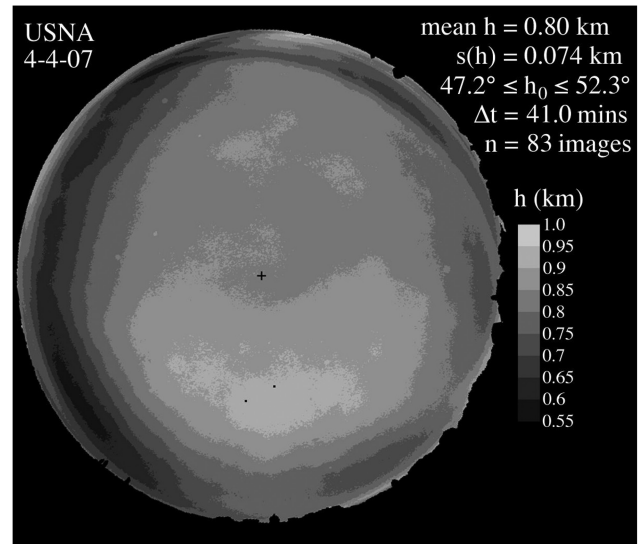

Fig. 21. Map of binned overcast h calculated from Fig. 4's measured $L(\theta, \phi_{rel})$ and MODTRAN simulated $L(\theta, h)$, with model parameters set to match the conditions observed at USNA on 4 April 2007. The mean $h = 0.80$ km and $s(h) = 0.0742$ km.

sured $L(\theta, \phi_{rel})$ and MODTRAN's simulated $L(\theta, h)$. Future research should incorporate independent, high-resolution measurements of z_{base} and h in order to vet our preliminary results. Nonetheless, Figs. 20 and 21 demonstrate the very real potential for making realistic ground-based measurements of overcast h in great angular detail.

5. Conclusions

Our research literally fills in some angular details missing from earlier work on overcast brightness distributions. Short-term temporal smoothing of fisheye images of overcast L and L_v lets us see both the small-scale irregularities peculiar to individual overcasts and the large-scale patterns common to many overcasts. Naturally, these insights are possible only after Section 2's rigorous radiometric and geometric calibration of our all-sky imaging system.

We have found common new overcast features such as the asymmetries in $L(\theta)$ that both (1) explain some apparent inconsistencies among earlier papers and (2) require new explanations of their own. Earlier differing opinions about the angular distribution of overcast L and L_v can now be seen as a problem of undersampling: if only a relatively few radiance measurements are available, then reconciling their patterns with the appealing (but usually incorrect) assumption of zenithal symmetry is nearly impossible. And although zenith-to-horizon profiles of overcast brightness remain useful, we now know a fundamental caveat about them: even for optically thick overcasts, brightness is seldom constant along almucantars. So Subsection 3.B's near-horizon behavior of $L(\theta)$ notwithstanding, meridional profiles of overcast brightnesses that are averaged over all ϕ_{rel} may obscure important details.

Fig. 20. Map of binned overcast thickness h calculated from Fig. 9's measured $L(\theta, \phi_{rel})$ and MODTRAN simulated $L(\theta, h)$, with model parameters set to match the conditions observed at USNA on 12 February 2008. The mean $h = 0.858$ km and its standard deviation $s(h) = 0.0598$ km.

Thus the simplest explanation for overcasts' $L(\theta)$ asymmetries is also one of the most obvious: real overcasts do not have spatially constant h, even when averaged over tens of minutes. Instead, changing gradients of h appear to variously tilt and distort the time-averaged patterns of $L(\theta)$, which themselves depend largely on paired increases in θ and slant-path τ through the overcast [27]. If only this $\tau(\theta)$ dependence governed overcast brightness, then zenithal symmetry would indeed be the norm. This fundamental new observation about overcasts may well be useful not only to researchers in atmospheric optics, but also to those in lighting engineering, animal navigation, and photosynthetic productivity.

References and Notes

1. M. Minnaert, *Light and Color in the Outdoors*, translated and revised by L. Seymour (Springer-Verlag, 1993), pp. 154–155.
2. P. Moon and D. E. Spencer, "Illumination from a non-uniform sky," Illum. Eng. **37**, 707–726 (1942).
3. Commission Internationale de l'Eclairage (CIE), *Spatial Distribution of Daylight—CIE Standard Overcast Sky and Clear Sky*, CIE Standard no. S 003/E-1996 (CIE, 1996).
4. R. L. Lee, Jr. and J. Hernández-Andrés, "Short-term variability of overcast brightness," Appl. Opt. **44**, 5704–5711 (2005).
5. We use "brightness" to connote either luminance or visible-wavelength radiance if no *qualitative* visual difference likely exists between the two. That said, we are well aware of the quantitative differences between these two photometric and radiometric measures of skylight energy; e.g., see G. Wyszecki and W. S. Stiles, *Color Science: Concepts and Methods, Quantitative Data and Formulae*, 2nd ed. (Wiley, 1982), pp. 259–260.
6. S. Fritz, "Illuminance and luminance under overcast skies," J. Opt. Soc. Am. **45**, 820–825 (1955).
7. F. C. Hooper and A. P. Brunger, "A model for the angular distribution of sky radiance," J. Sol. Energy Eng. **102**, 196–202 (1980).
8. M. A. Rosen and F. C. Hooper, "A comparison of two models for the angular distribution of diffuse sky radiance for overcast skies," Sol. Energy **42**, 477–482 (1989).
9. N. Igawa, Y. Koga, T. Matsuzawa, and H. Nakamura, "Models of sky radiance distribution and sky luminance distribution," Sol. Energy **77**, 137–157 (2004).
10. M. D. Steven and M. H. Unsworth, "The angular distribution and interception of diffuse solar radiation below overcast skies," Q. J. R. Meteorol. Soc. **106**, 57–61 (1980).
11. D. Enarun and P. Littlefair, "Luminance models for overcast skies: assessment using measured data," Int. J. Lighting Res. Technol. **27**, 53–58 (1995).
12. A. Bartzokas, S. Darula, H. D. Kambezidis, and R. Kittler, "Sky luminance distribution in central Europe and the Mediterranean area during the winter period," J. Atmos. Sol.-Terr. Phys. **65**, 113–119 (2003).
13. D. H. Li, C. C. Lau, and J. C. Lam, "Overcast sky conditions and luminance distribution in Hong Kong," Build. Environ. **39**, 101–108 (2004).
14. T. Muneer, "Evaluation of the CIE overcast sky model against Japanese data," Energy Build. **27**, 175–177 (1998).
15. J. I. Gordon and P. V. Church, "Overcast sky luminances and directional luminous reflectances of objects and backgrounds under overcast skies," Appl. Opt. **5**, 919–923 (1966).
16. R. Kittler and P. Valko, "Radiance distribution on densely overcast skies: comparison with CIE luminance standard," Sol. Energy **51**, 349–355 (1993).
17. R. H. Grant and G. M. Heisler, "Obscured overcast sky radiance distributions for ultraviolet and photosynthetically active radiation," J. Appl. Meteorol. **36**, 1336–1345 (1997).
18. R. Perez, R. Seals, and J. Michalsky, "All-weather model for sky luminance distribution—preliminary configuration and validation," Sol. Energy **50**, 235–245 (1993)
19. R. Perez, R. Seals, and J. Michalsky, "Erratum to all-weather model for sky luminance distribution—preliminary configuration and validation," Sol. Energy **51**, 423 (1993).
20. Commission Internationale de l'Eclairage, *Spatial Distribution of Daylight—CIE Standard General Sky* CIE Standard no. S 011/E:2003 (CIE, 2003).
21. C. A. Coombes and A. W. Harrison, "Angular distribution of overcast sky short wavelength radiance," Sol. Energy **40**, 161–166 (1988).
22. A. W. Harrison, "Directional sky luminance versus cloud cover and solar position," Sol. Energy **46**, 13–19 (1991).
23. R. H. Grant, G. M. Heisler, and W. Gao, "Ultraviolet sky radiance distributions of translucent overcast skies," Theor. Appl. Climatol. **58**, 129–139 (1997).
24. A. Soler and L. Robledo, "Investigation of the overcast skies luminance distribution using 35 sensors fixed on a dome," Energy Convers. Manage. **46**, 2739–2747 (2005).
25. S. Wuttke and G. Seckmeyer, "Spectral radiance and sky luminance in Antarctica: a case study," Theor. Appl. Climatol. **85**, 131–148 (2006).
26. R. L. Lee, Jr., and J. Hernández-Andrés, "Colors of the daytime overcast sky," Appl. Opt. **44**, 5712–5722 (2005).
27. R. L. Lee, Jr., "Measuring overcast colors with all-sky imaging," Appl. Opt. **47**, H106–H115 (2008).
28. For examples of overcast L distributions from individual photographs, see Figs. 3–4 in E. G. Rossini and A. Krenzinger, "Maps of sky relative radiance and luminance distributions acquired with a monochromatic CCD camera," Sol. Energy **81**, 1323–1332 (2007).
29. J. L. Nieves, E. M. Valero, S. M. C. Nascimento, J. Hernández-Andrés, and J. Romero, "Multispectral synthesis of daylight using a commercial digital CCD camera," Appl. Opt. **44**, 5696–5703 (2005).
30. Photo Research, Inc., 9731 Topanga Canyon Place, Chatsworth, Calif. 91311. The PR-650's spectral range is 380–780 nm, its step size is 4 nm, and its telescopic lens permits radiance measurements across a 1° diameter FOV.
31. D. Wüller and H. Gabele, "The usage of digital cameras as luminance meters," Proc. SPIE **6502**, 65020U (2007).
32. Clearly $\sin(\theta_i) = r_n$ cannot describe exactly the projection of a nominally orthographic lens that forms images at $\theta_i > 90°$ where $r_n > 1$.
33. K. J. Voss and G. Zibordi, "Radiometric and geometric calibration of a visible spectral electro-optic 'fisheye' camera radiance distribution system," J. Atmos. Ocean. Technol. **6**, 652–662 (1989).
34. Although the FC-E8 FOV actually exceeds 180° by a few degrees, we ignore all pixels below the astronomical horizon as irrelevant to our interests here. In actual practice, topography seen from our USNA rooftop site obstructs the lowest 1° or so of the sky.
35. T. S. Glickman, ed., *Glossary of Meteorology*, 2nd ed. (American Meteorological Society, 2000), pp. 390, 694.

36. C. F. Bohren and A. B. Fraser, "Colors of the sky," Phys. Teach. **23**, 267–272 (1985).

37. R. L. Lee, Jr., "Horizon brightness revisited: measurements and a model of clear-sky radiances," Appl. Opt. **33**, 4620–4628, 4959 (1994).

38. J. Li, J. W. Geldart, and P. Chylek, "Solar radiative transfer in clouds with vertical internal inhomogeneity," J. Atmos. Sci. **51**, 2542–2552 (1994).

39. A. Los and P. G. Duynkerke, "Microphysical and radiative properties of inhomogeneous stratocumulus: observations and model simulations," Q. J. R. Meteorol. Soc. **126**, 3287–3307 (2000).

40. A. A. Kokhanovsky, "The influence of horizontal inhomogeneity on radiative characteristics of clouds: an asymptotic case study," IEEE Trans. Geosci. Remote Sens. **41**, 817–825 (2003).

41. Y. Chen, K. N. Liou, and Y. Gu, "An efficient diffusion approximation for 3D radiative transfer parameterization: application to cloudy atmospheres," J. Quant. Spectrosc. Radiat. Transf. **92**, 189–200 (2005).

42. A. Kylling, A. R. Webb, R. Kift, G. P. Gobbi, L. Ammannato, F. Barnaba, A. Bais, S. Kazadzis, M. Wendisch, E. Jäkel, S. Schmidt, A. Kniffka, S. Thiel, W. Junkermann, M. Blumthaler, R. Silbernagl, B. Schallhart, R. Schmitt, B. Kjeldstad, T. M. Thorseth, R. Scheirer, and B. Mayer, "Spectral actinic flux in the lower troposphere: measurement and 1-D simulations for cloudless, broken cloud and overcast situations," Atmos. Chem. Phys. **5**, 1975–1997 (2005).

43. G. P. Anderson, A. Berk, P. K. Acharya, M. W. Matthew, L. S. Bernstein, J. H. Chetwynd, H. Dothe, S. M. Adler-Golden, A. J. Ratkowski, G. W. Felde, J. A. Gardner, M. L. Hoke, S. C. Richtsmeier, B. Pukall, J. Mello, and L. S. Jeong, "MODTRAN4: radiative transfer modeling for remote sensing," Proc. SPIE **4049**, 176–183 (2000).

44. Our MODTRAN4 simulations use (1) the model's default single-scattering properties for each cloud type and for boundary-layer aerosols, (2) a 23 km surface visual range, (3) a spectral interval of 400–700 nm, (4) a locally measured surface air temperature, and (5) a surface Lambertian albedo of 0.2. Although a nearby ceilometer measured z_{base}, we could find no comparable data on cloud top heights that met our temporal and spatial requirements (i.e., samples at intervals of 30 s and 50–100 m).